Journal of Himalayan Earth Sciences Volume 59, No. 1, 2026 pp. 34-50

Surface Heat Flux Variability Associated with Coupled Indian and Pacific Subtropical Highs

Nasir Ilyas[1,2*] and Muhammad Jawed Iqbal[1]

[1] Institute of Space Science and Technology (ISST), University of Karachi, Karachi, Pakistan
[2] Department of Physics, Government Delhi College, Sindh Education Department, Karachi, Pakistan
**Corresponding Author: nasir.ilyaaz@gmail.com*

Submitted Date:22/09/2025 Acceptance Date: 12/12/2025 Publication Date: 31/03/2026

Abstract

This study investigates the combined influence of the Indian Ocean High Pressure (IOHP) and South Pacific High Pressure (SPH) systems on Southern Hemisphere summer (December–January–February; DJF) surface heat fluxes and regional thermal conditions over the southeastern Indian Ocean and eastern Australia during 1988–2017. Using the Center of Action (COA) framework, years were classified into combined phases, identifying six HH (high IOHP–high SPH) and six LL (low IOHP–low SPH) years. Composite analyses reveal that HH years exhibit drier air, suppressed evaporation, and reduced latent heat flux (LHF), alongside moderate increases in sensible heat flux (SHF), enhancing near-surface warming. Thermodynamic anomalies (Qa, Qs, Ta, Ts) overlaid with wind vectors indicate enhanced boundary-layer stability and strengthened easterly to southeasterly flow, limiting onshore moisture transport and confirming weaker air–sea interaction during HH phases. Correlation analyses show a significant negative association between IOHP and LHF ($r = –0.38$, $p < 0.05$) and a positive spatial coupling between IOHP longitude and SPH pressure ($r = 0.40$, $p < 0.05$), highlighting the role of subtropical highs in modulating surface fluxes. Detrended spatial correlations further indicate that IOHP–SPH coupling acts as the primary driver of LHF and SHF variability, while broader climate modes—Southern Annular Mode (SAM), Indian Ocean Dipole (IOD), and El Niño–Southern Oscillation (ENSO; Niño 3.4 and Niño 4)—exert secondary, regionally modulated influences on surface fluxes and seasonal skin temperature. Spatial trend analyses reveal declining LHF across the subtropical southeast Indian Ocean, heterogeneous SHF patterns, and subtle sea-level pressure increases, suggesting potential IOHP intensification. Monte Carlo and bootstrapped tests confirm the robustness of these results. Overall, coupled subtropical highs dominate regional ocean–atmosphere energy exchange and surface heating patterns, providing a process-level understanding of how circulation anomalies amplify summer climate extremes in a warming climate.

***Keywords*:** Subtropical highs; IOHP; SPH; Latent heat flux; Sensible heat flux; DJF; Ocean–atmosphere interactions; SAM; IOD; ENSO; Composite analysis

1. Introduction

Australia's climate has warmed rapidly in recent decades, marked by more frequent and intense summer (DJF) heatwaves (Alexander and Arblaster, 2009; Lewis et al., 2017). Persistent high-pressure systems strongly influence the surface energy balance on seasonal and interannual timescales (Holbrook et al., 2022; Trenberth and Fasullo, 2012). Among these, the Indian Ocean High (IOHP) and South Pacific High (SPH) are key subtropical anticyclones shaping climate over southern and eastern Australia (Hameed et al., 2011; Pepler et al., 2019; Ur Rehman et al., 2024). By steering moisture transport and strengthening easterly–southeasterly flow, these highs restrict onshore moisture, enhance dry advection, and intensify near-surface warming (Arblaster et al., 2011; Zhang et al.,

1997). Regional studies have reported significant inter-annual variability in rainfall and temperature across Pakistan and the broader Himalayan region (Khattak and Ali, 2015; Khan et al., 2022; Yaseen et al., 2015), underscoring the need to better understand underlying thermodynamic and circulation controls on surface heat-flux variability.

While earlier studies have examined their individual effects, the combined influence of IOHP and SPH on surface turbulent heat fluxes—latent (LHF) and sensible (SHF)—remains underexplored (Balsamo et al., 2009; Holbrook et al., 2022; Zhao and Wang, 2017). Addressing this gap, the present work applies a Center of Action (COA) framework over the IOHP and SPH domains (10–45° S, 60–120° E) for DJF 1988–2017. Combined phases (HH: High IOHP–High SPH; LL: Low IOHP–Low SPH) were defined using pressure, latitude, and longitude indices (Romanski and Hameed, 2015). Composite differences in LHF, SHF, thermodynamic gradients (Qa–Qs, Ta–Ts), and winds were evaluated using Monte Carlo significance testing (Wilks, 2016).

These diagnostics provide a process-based understanding of how coupled subtropical highs regulate surface energy exchange and amplify summer heat extremes over Australia and surrounding oceans.

Unlike earlier investigations that emphasized rainfall anomalies and moisture convergence (Holbrook et al., 2019; Pepler et al., 2014), the present study concentrates on surface turbulent heat-flux variability and its thermodynamic and dynamic controls. By applying the Center-of-Action (COA) framework to the coupled Indian and South Pacific subtropical highs, we focus on energy-exchange mechanisms (latent and sensible heat fluxes, Qa–Qs, Ta–Ts) that modulate boundary-layer stability and precede rainfall responses. This flux-centric approach, therefore, extends previous precipitation-based analyses to the underlying physical drivers of regional climate variability.

2. Methodology

2.1 Data Sources and Temporal Scope

The study examines the austral summer (DJF) seasons from 1988 to 2017. Latent (LHF) and sensible (SHF) heat fluxes were obtained from the OAFlux dataset (1° × 1°; Yu and Weller, 2007), while sea-level pressure (SLP), near-surface air temperature (Ta), sea-surface temperature (Ts), 2 m specific humidity (Qs), 850 hPa humidity (Qa), and wind (U, V) fields were taken from the NCEP/NCAR Reanalysis-I (Kalnay et al., 1996).

ENSO (Niño 3.4), Southern Annular Mode (SAM; Marshall, 2003), and Indian Ocean Dipole (IOD; Saji et al., 1999) Indices were sourced from NOAA and JAMSTEC. All datasets were detrended before correlation and composite analyses to isolate interannual variability. The analysis domain spans 60° E – 180° E and 45° S – 10° S, covering the southeastern Indian Ocean and eastern Australia.

2.2 IOHP and SPH Indices Based on the COA Method

To quantify the spatial characteristics of the Indian Ocean High Pressure (IOHP) and South Pacific High (SPH) systems, the Center of Action (COA) framework was applied over their respective domains. For each DJF season, three indices were computed based on the deviation of sea level pressure (SLP) from a fixed threshold (Pt = 1020 hPa): the Pressure Index, Latitude Index, and Longitude Index, following the methodology adapted from (Romanski and Hameed, 2015). The formulas used are as follows:

Pressure Index:

$$\boldsymbol{I_{P,\Delta t}} = \frac{\sum_{i=1}^{I}\sum_{j=1}^{J}(\boldsymbol{P_{ij}} - \boldsymbol{P_t})\ \cos\boldsymbol{\varphi_{ij}}\ \boldsymbol{\delta_{ij}}}{\sum_{i=1}^{I}\sum_{j=1}^{J}\ \cos\boldsymbol{\varphi_{ij}}\ \boldsymbol{\delta_{ij}}} \quad \text{……..(1)}$$

Latitude Index:

$$\boldsymbol{I_{\emptyset\,,\Delta t}} = \frac{\sum_{i=1}^{I}\sum_{j=1}^{J}(\boldsymbol{P_{ij}} - \boldsymbol{P_t})\ \emptyset_{ij}\ \ \cos\boldsymbol{\varphi_{ij}}\ \boldsymbol{\delta_{ij}}\emptyset_{ij}}{\sum_{i=1}^{I}\sum_{j=1}^{J}(\boldsymbol{P_{ij}} - \boldsymbol{P_t})\cos\boldsymbol{\varphi_{ij}}\ \boldsymbol{\delta_{ij}}} \quad \text{……..(2)}$$

Longitude Index:

$$I_{\lambda,\Delta t} = \frac{\sum_{i=1}^{I}\sum_{j=1}^{J}(P_{ij} - P_t)\ \lambda_{ij}\ \cos\varphi_{ij}\ \delta_{ij}\emptyset_{ij}}{\sum_{i=1}^{I}\sum_{j=1}^{J}(P_{ij} - P_t)\cos\varphi_{ij}\ \delta_{ij}} \quad \ldots\ldots\ldots(3)$$

These indices are denoted as IOH_P, IOH_LAT, and IOH_LON for the Indian Ocean High, and SPH_P, SPH_LAT, and SPH_LON for the South Pacific High. Latitude and longitude indices were computed similarly using their respective coordinate weights.

Where

- P_{ij} is the DJF sea level pressure at grid point (i, j).
- P_t = 1020 hPa is the pressure threshold.
- ϕ_{ij} and λ_{ij} are the latitude and longitude of the grid point (i, j), respectively
- δ_{ij} is a binary mask that equals 1 if (P_{ij} - P_t) > 0, and 0 otherwise
- All Σ are over ocean grid points within the study domain D = (60°E–180°E, 45°S–10°S)
- Δt denotes the seasonal averaging window (DJF).

2.3 Classification of Combined Phases

DJF years were grouped into four IOHP–SPH phases based on standardized SLP anomalies (z ≥ +0.5 for high, ≤ –0.5 for low). Composite analysis used only the HH (IOHP-High/SPH-High) and LL (IOHP-Low/SPH-Low) years; neutral and mixed cases were excluded. (Pepler et al., 2019; Romanski and Hameed, 2015).

2.4 Composite and Thermodynamic Diagnostics

Composite differences (HH–LL) were computed for LHF, SHF, temperature (Ta–Ts), wind (U, V) fields, and specific humidity (Qa–Qs). These diagnostics describe how variations in subtropical pressure centers alter moisture transport, circulation, and surface energy exchange.

2.5 Monte Carlo Significance Testing

Statistical robustness was assessed using a Monte Carlo permutation test (Wilks, 2016) with 1,000 random re-groupings of HH and LL years. Regions exceeding the 95th percentile ($p \leq 0.05$) were considered significant and marked by stippling.

3. Results

3.1 Phase Classification Overview

The phases of the IOHP and SPH systems were classified based on their standardized anomalies (z-scores) during the period 1988–2017. The mean and standard deviation for each system were calculated as follows:

- IOHP Mean SLP: 1018.70 hPa (Standard Deviation = 0.40 hPa)
- SPH Mean SLP: 1018.82 hPa (Standard Deviation = 0.55 hPa)

Using these values, we classified each year into high, low, and neutral phases based on the z-scores calculated for each year's sea level pressure (SLP). The thresholds used for phase classification were +0.5 for high phases, -0.5 for low phases, and values in between were considered neutral.

3.1.1. Combined Phases (1988–2017)

Table 1 summarizes the occurrence of each combined phase of IOHP and SPH during the DJF season from 1988 to 2017.

Table 1: Combined Phase Occurrences of IOHP and SPH during the DJF Season (1988–2017).

Phase Type	Number of Years
HH (High IOHP – High SPH)	6
HL (High IOHP – Low SPH)	7
LH (Low IOHP – High SPH)	5
LL (Low IOHP – Low SPH)	6
Neutral (All Other Cases)	6

3.2 Long-Term Trends of Atmospheric and Oceanic Indices

To explore the temporal evolution of atmospheric systems and teleconnection indices over the study period (1988–2017), we computed the Pearson correlation of each variable with time. While most indices exhibit weak or statistically insignificant trends, the latitude of the IOHP shows a moderate positive correlation (r = 0.308, p =

0.098), suggesting a potential poleward shift of the high-pressure system. Similarly, SHF shows a borderline negative trend (r = -0.330, p = 0.075), possibly linked to changes in surface energy balance due to shifting atmospheric dynamics. Other variables, such as IOHP pressure, SPH pressure, and ENSO indices, did not demonstrate statistically significant long-term trends.

Table 2: Pearson correlation coefficients between key variables and time (1988–2017). Significant values approaching $p < 0.05$ are italicized.

Variable	Correlation coefficient with time (r)	p-value
IOHP	0.209	0.268
IOHP Latitude	0.308	0.098
IOHP Longitude	-0.014	0.94
SPH	0.166	0.381
SPH Latitude	0.183	0.333
SPH Longitude	-0.008	0.965
SAM	-0.063	0.741
IOD	-0.177	0.35
Nino 3.4	0.045	0.814
Nino 4	-0.122	0.519
LHF	0.111	0.56
SHF	-0.33	0.075

Note: Negative correlations denote declining trends in latent or sensible heat fluxes over time, while positive correlations indicate increasing fluxes or pressure intensification consistent with subtropical high strengthening.

3.3 Interrelationship Among Teleconnection Indices

To assess inter-variable connectivity, a Pearson correlation matrix was computed for all atmospheric pressure, positional, and teleconnection indices. Statistically significant correlations ($p < 0.05$) are highlighted in bold with an asterisk (*). *Notably, IOHP and LHF exhibit a significant negative correlation (r = -0.38*), indicating suppression of latent heat flux under stronger high-pressure regimes. Additionally, IOHP longitude shows strong alignment with SPH pressure (r = 0.40*), suggesting spatial coupling in subtropical high positioning.

3.4 Spatial Trends in Surface Heat Fluxes and Pressure Fields.

Building upon the temporal relationships discussed above, we further analyzed the spatial trends in surface latent heat flux (LHF), sensible heat flux (SHF), and sea level pressure (SLP) over the southeastern Indian Ocean and surrounding regions for the DJF season (1988–2017). This approach allows us to visualize regional patterns and identify zones of statistically significant change.

The trend maps for LHF (Fig. 2a) and SHF (Fig. 2b) reveal distinct spatial signatures. A notable declining trend in LHF is observed across the subtropical southeast Indian Ocean, aligning with areas under the influence of the IOHP. This pattern supports the earlier finding of a negative correlation between IOHP strength and LHF variability. In contrast, SHF trends are generally weaker but exhibit isolated zones of both positive and negative tendencies.

The corresponding SLP trend field (Fig. 2c) indicates subtle increases in pressure over the same region, suggesting a potential intensification or spatial expansion of the IOHP. While not all trends are statistically significant at the 95% confidence level, the spatial coherence among the LHF, SHF, and SLP trends highlights the possible coupling between surface fluxes and high-pressure dynamics.

3.5 Detrended Spatial Correlation Analysis with Centers of Action (COA: IOHP, SPH)

The spatial detrended correlations are computed between two major atmospheric centers of action (IOHP, SPH) and surface heat fluxes (LHF and SHF), using DJF data from 1988–2017. This approach removes linear trends from the time series at each grid point, ensuring that only inter-annual variability is assessed.

Table 3: Correlation matrix of atmospheric and teleconnection variables (1988–2017). Bold values with an asterisk (*) are statistically significant at $p < 0.05$. Positive correlations between IOHP and SPH indices indicate synchronous strengthening of the subtropical highs, while significant links with ENSO, IOD, and SAM highlight how large-scale teleconnections modulate high-pressure variability and associated surface fluxes.

Variables	IOHP	IOHP Latitude	IOHP Longitude	SPH	SPH Latitude	SPH Longitude	SAM	IOD	Niño 3.4	Niño 4	LHF	SHF
IOHP	1	0.17	-0.23	-0.06	-0.14	0.17	0.21	0.21	-0.2	-0.03	**-0.38***	0.08
IOHP Lat	0.17	1	0.09	0.06	0.03	-0.27	-0.19	-0.11	-0.03	0.28	-0.09	-0.06
IOHP Lon	-0.23	0.09	1	0.4	0	0.09	-0.16	0.26	-0.01	0.06	-0.11	-0.04
SPH	-0.06	0.06	**0.4***	1	0.15	-0.14	-0.04	-0.11	-0.23	0.09	-0.14	0.18
SPH Lat	-0.14	0.03	0	0.15	1	0.17	-0.06	-0.25	0.08	-0.21	0.08	-0.07
SPH Lon	0.17	-0.27	0.09	-0.14	0.17	1	-0.05	0.25	-0.13	0	-0.19	-0.11
SAM	0.21	-0.19	-0.16	-0.04	-0.06	-0.05	1	-0.19	-0.25	-0.28	-0.13	-0.07
IOD	0.21	-0.11	0.26	-0.11	-0.25	0.25	-0.19	1	0.23	0.33	-0.1	-0.07
Niño 3.4	-0.2	-0.03	-0.01	-0.23	0.08	-0.13	-0.25	0.23	1	0.81	-0.11	0.04
Niño 4	-0.03	0.28	0.06	0.09	-0.21	0	-0.28	0.33	0.81	1	-0.05	0.01
LHF	-0.38	-0.09	-0.11	-0.14	0.08	-0.19	-0.13	-0.1	-0.11	-0.05	1	0.34
SHF	0.08	-0.06	-0.04	0.18	-0.07	-0.11	-0.07	-0.07	0.04	0.01	0.34	1

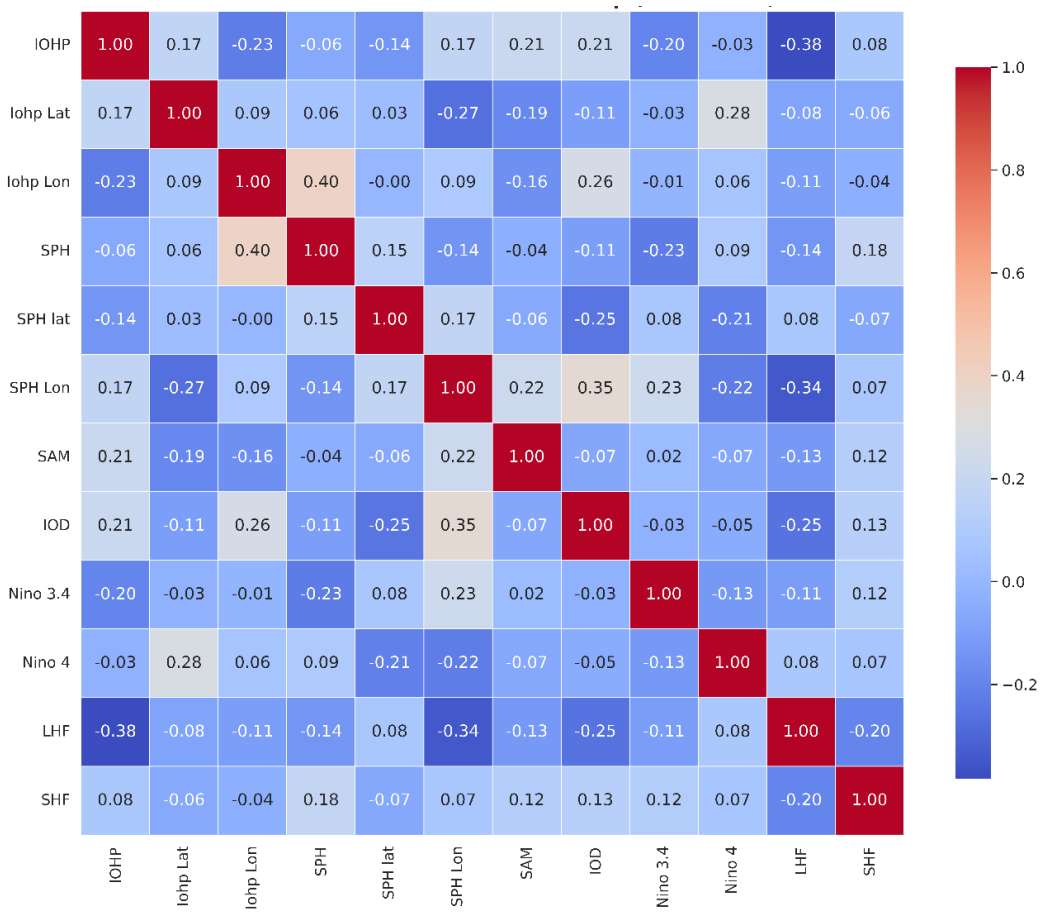

Fig. 1. Color-coded correlation heat-map among atmospheric variables and indices during 1988–2017. Warm colors indicate positive correlation; cool colors indicate negative correlation. Significant patterns are emphasized in the discussion.

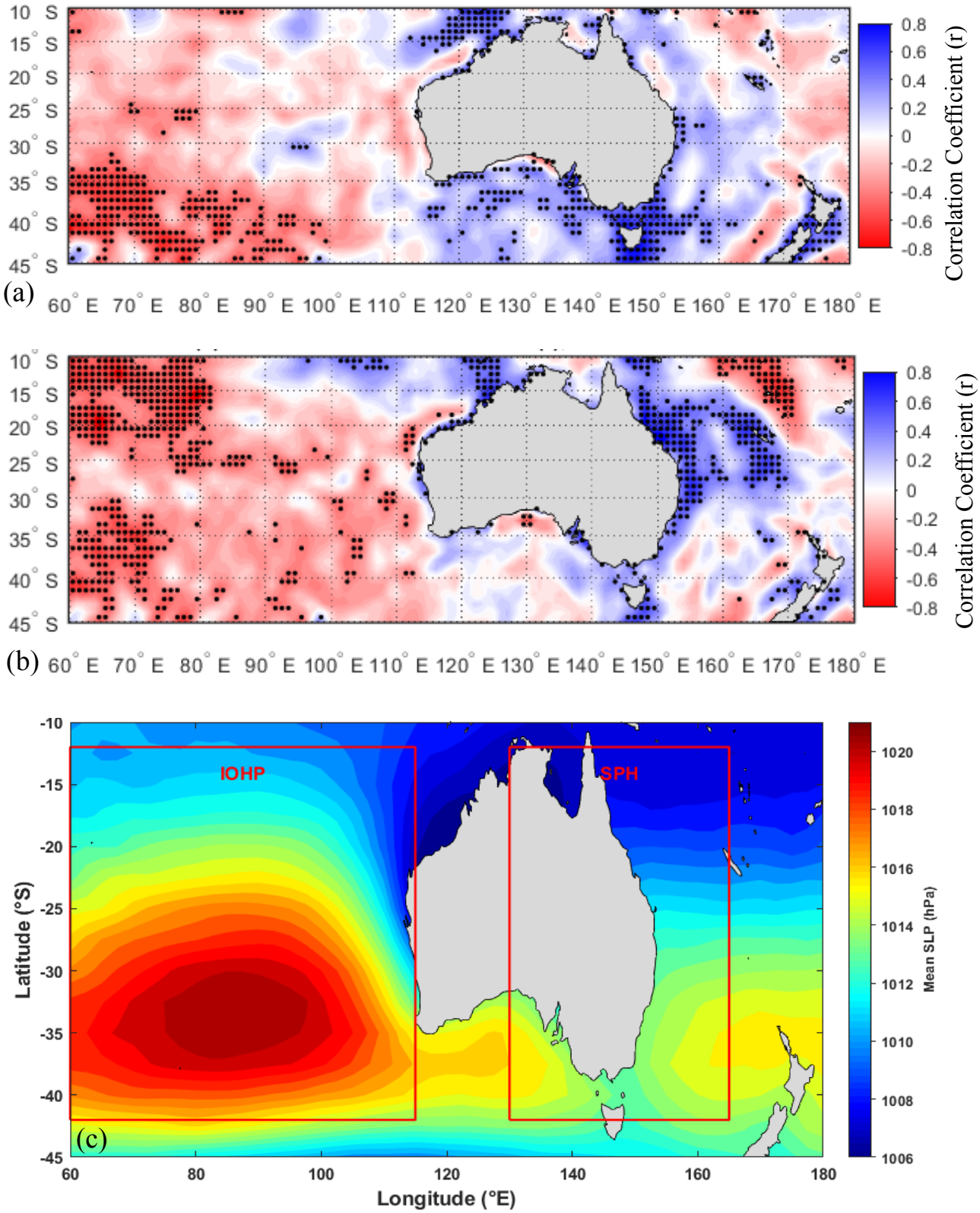

Fig. 2. (a) Spatial correlation between time and latent heat flux (LHF) during DJF (1988–2017), with Monte Carlo-based significance masking ($p < 0.05$; 1,000 iterations), (b) Same as (a), but for sensible heat flux (SHF), (c) Mean DJF Sea level pressure (SLP; hPa) over the southeastern Indian Ocean and Australia during 1988–2017, highlighting the Indian Ocean High Pressure (IOHP: 60°–120°E, 10°–45°S) and South Pacific High (SPH: 140°–180°E, 10°–45°S) regions with red boxes. Color shading indicates SLP magnitude, with warmer colors (yellow–red) representing higher pressure.

The results reveal significant negative correlations between LHF and IOHP (Fig. 3a), particularly over the southeastern Indian Ocean, suggesting suppressed evaporation under stronger IOHP regimes. SHF also exhibits a strong negative correlation with IOHP (Fig. 3b), indicating reduced surface turbulent heat transfer under enhanced subsidence. Over the western Pacific, LHF is moderately anti-correlated with SPH (Fig. 3c), while SHF shows scattered but statistically significant inverse relations with SPH influence zones (Fig. 3d). These findings underscore the dynamic influence of semi-permanent high-pressure systems on regional ocean-atmosphere energy coupling.

The influence of two major atmospheric centers of action (IOHP, SPH) is assessed on seasonal mean skin temperature (Ts) over DJF 1988–2017. Using spatially detrended time series to remove linear trends at each grid point, we computed bootstrapped Pearson correlations (10,000 resamples) to quantify inter-annual associations robustly. The results reveal a negative correlation between IOHP and Ts ($r = –0.343$, $p = 0.0632$; bootstrapped $r = –0.350$, 95% CI: –0.616 to –0.006), while SPH exhibits a moderate positive correlation with Ts ($r = 0.368$, $p = 0.0455$; bootstrapped $r = 0.349$, 95% CI: 0.014 to 0.623). These correlations confirm that variations in semi-permanent high-pressure systems significantly modulate regional surface thermal conditions, supporting the patterns observed in latent and sensible heat fluxes and highlighting their role in ocean–atmosphere energy coupling.

3.6 Detrended Spatial Correlation with SAM and IOD

To evaluate the broader climate teleconnections, we performed detrended spatial correlation analysis between surface heat fluxes and two additional indices: the Southern Annular Mode (SAM) and the Indian Ocean Dipole (IOD). These patterns help reveal how variations in these large-scale modes influence surface energy fluxes across the Australian and Indo-Pacific domain.

As shown in Fig. 4, the SAM-related maps (panels a and b) reveal that both LHF and SHF exhibit regionally varied patterns of correlation, with a general tendency for weak to moderate negative correlations over southern latitudes, particularly near the mid-latitude westerlies. The IOD-related maps (panels c and d) display stronger and more coherent correlations, especially over the eastern Indian Ocean, where positive IOD phases tend to suppress latent heat flux, consistent with drier and cooler SST anomalies in the eastern pole. Sensible heat flux patterns show weaker, scattered correlations with IOD, suggesting its secondary role in regulating surface heating.

3.7 Detrended Spatial Correlation with ENSO

To assess the influence of ENSO variability on surface turbulent heat fluxes, we analyzed the detrended correlation of LHF and SHF with the Niño 3.4 index during DJF (1988–2017). This index is central to western Pacific SST anomalies and plays a crucial role in modulating atmospheric convection and teleconnections across the Indo-Pacific sector.

As shown in Fig. 5, the Niño 3.4 index exhibits an extensive and coherent correlation pattern with LHF (panel a), showing widespread suppression across the Indian Ocean and enhanced evaporation over the central and western Pacific. SHF correlations (panel b) reinforce these patterns but are generally weaker in magnitude, highlighting eastern Australia's sensitivity to central-Pacific warming and its coupling with the South Pacific High.

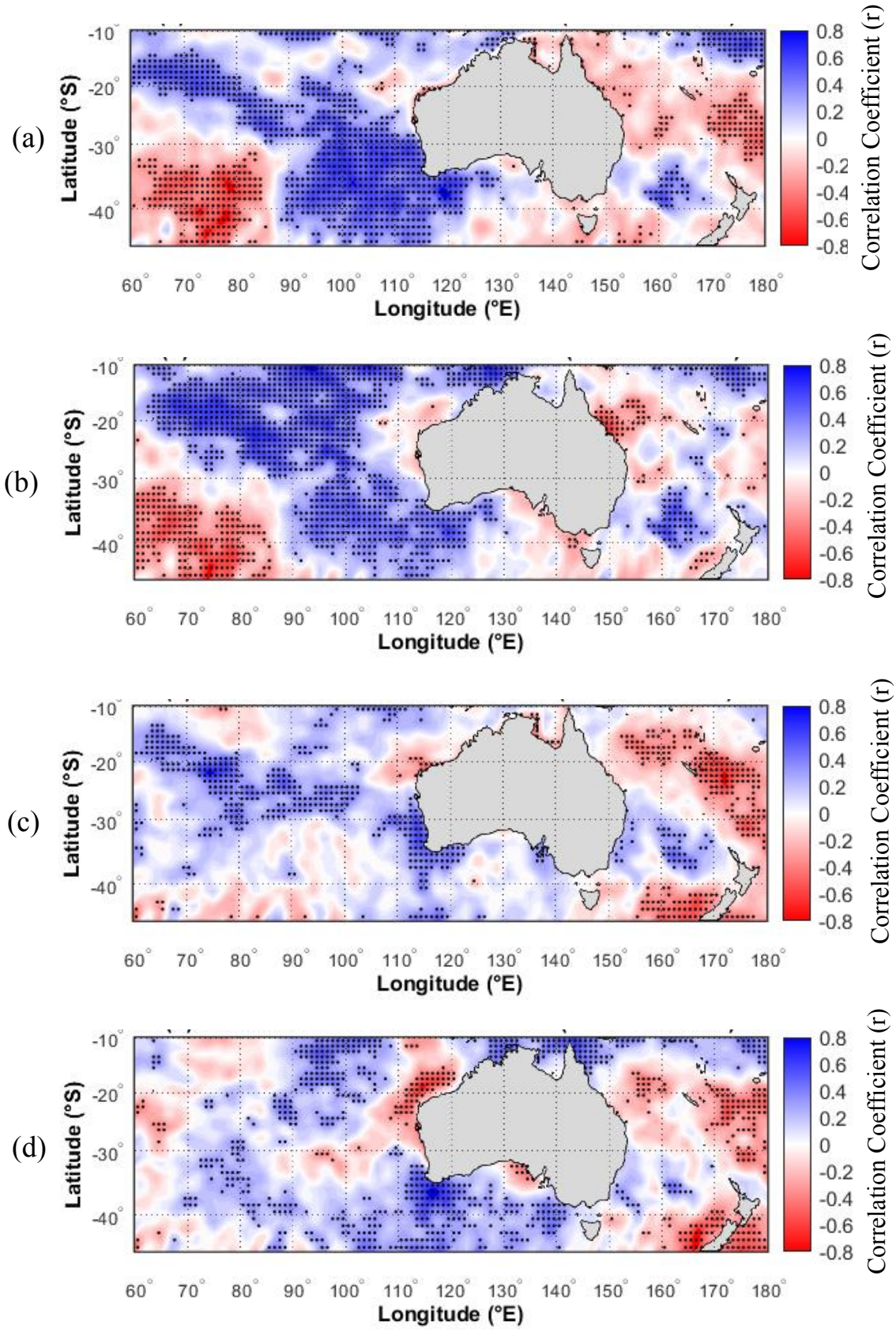

Fig. 3. Detrended spatial correlation between high-pressure systems and surface heat fluxes during DJF (1988–2017): (a) LHF vs IOHP, (b) SHF vs IOHP, (c) LHF vs SPH, and (d) SHF vs SPH. Blue shades denote positive correlations, red indicates negative. Stippling highlights regions where the correlation is statistically significant at $p < 0.05$.

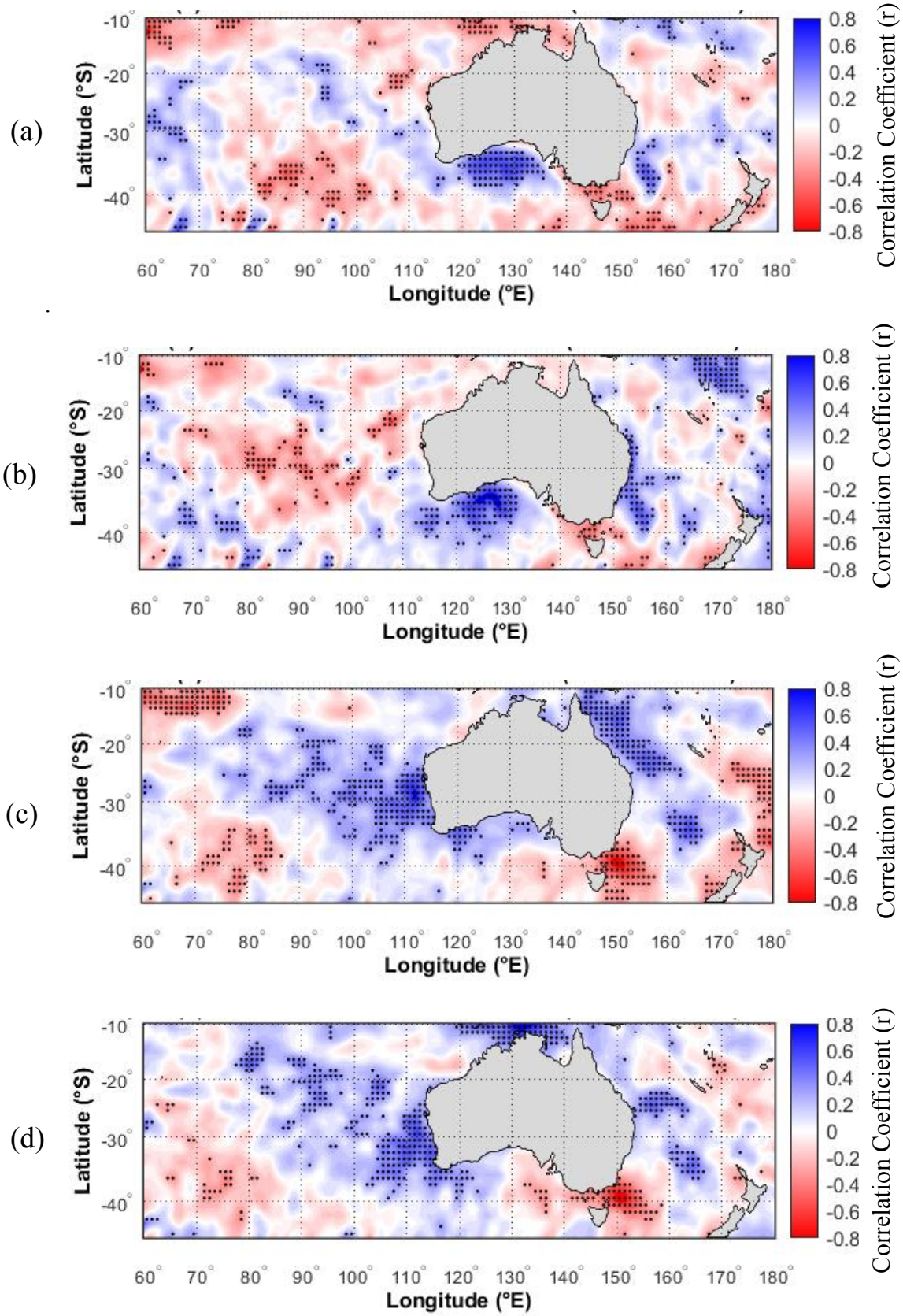

Fig. 4. Detrended spatial correlation between climate indices and surface heat fluxes during DJF (1988–2017): (a) LHF vs SAM, (b) SHF vs SAM, (c) LHF vs IOD, and (d) SHF vs IOD. Blue shades indicate positive correlation and red indicates negative. Stippling denotes significance at $p < 0.05$.

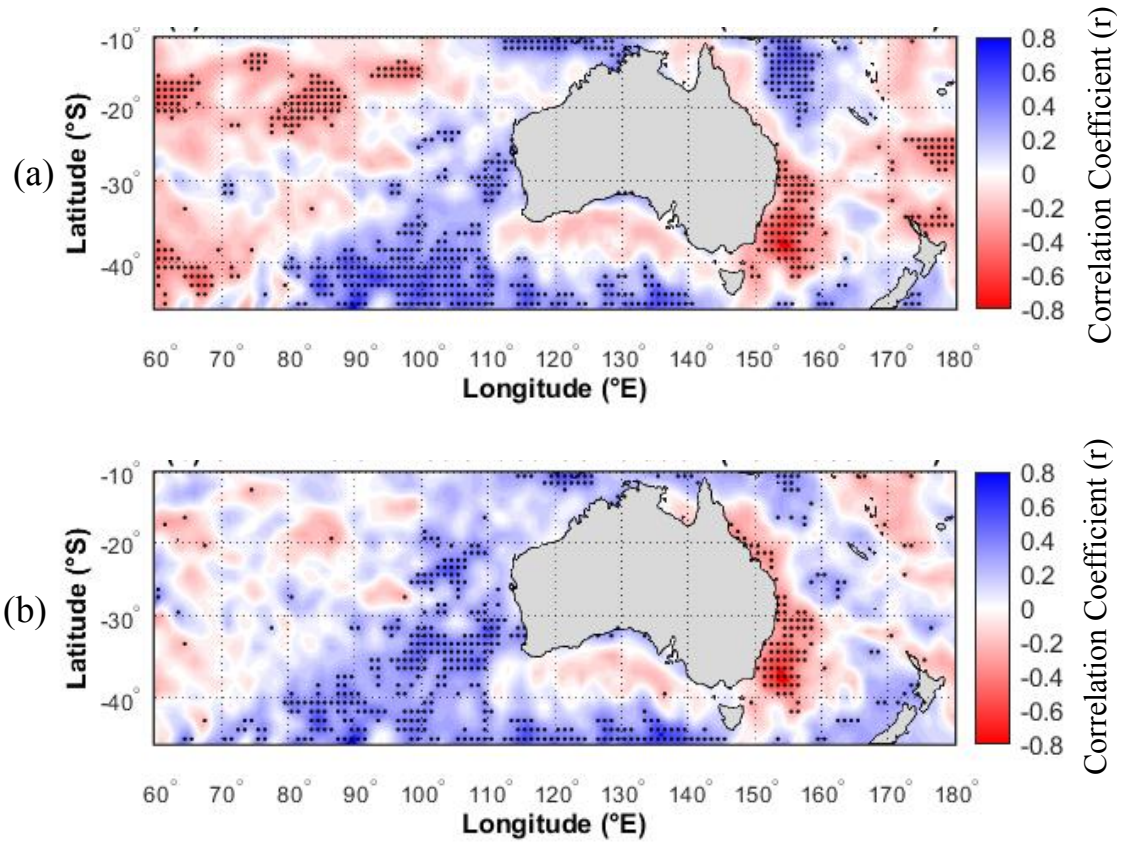

Fig. 5. Detrended spatial correlation between ENSO indices and surface heat fluxes during DJF (1988–2017): (a) LHF vs Niño 3.4, (b) SHF vs Niño 3.4. Blue indicates positive correlation and red indicates negative. Stippling highlights significant areas ($p < 0.05$).

3.8 HH–LL Composite Differences in Surface Heat Fluxes

Figure 6 displays the composite differences in surface heat fluxes (latent and sensible) between HH (High IOHP–High SPH) and LL (Low IOHP–Low SPH) years during the DJF season (1988–2017). Panel (a) highlights regions where LHF anomalies are most pronounced, particularly over the southeastern Indian Ocean, showing substantial suppression under HH phases. Panel (b) illustrates SHF differences, which exhibit moderate but spatially coherent patterns. Statistically significant areas (Monte Carlo, $p < 0.05$) are denoted by black hatching.

These composite patterns directly reflect the combined phase classification of IOHP and SPH (Section 3.1) and are consistent with the negative correlation between IOHP and LHF identified in Section 3.3 ($r = –0.38$*), confirming that stronger high-pressure regimes inhibit surface evaporation. The spatial structure of suppressed LHF aligns with long-term declining trends in latent heat flux over the southeastern Indian Ocean (Section 3.4), reinforcing the role of coupled highs in modulating the regional surface energy budget.

Furthermore, the anomalies in LHF and SHF correspond closely with the thermodynamic and circulation changes revealed in Sections 3.9–3.10: negative Qa–Qs gradients, enhanced boundary-layer stability (positive Ta–Ts), and strengthened easterly and southeasterly winds collectively restrict moisture transport toward Australia. These findings indicate that surface heat flux responses are not isolated phenomena but are tightly linked to the intensity, positioning, and coupling of subtropical highs**,** providing a mechanistic explanation for observed energy flux anomalies.

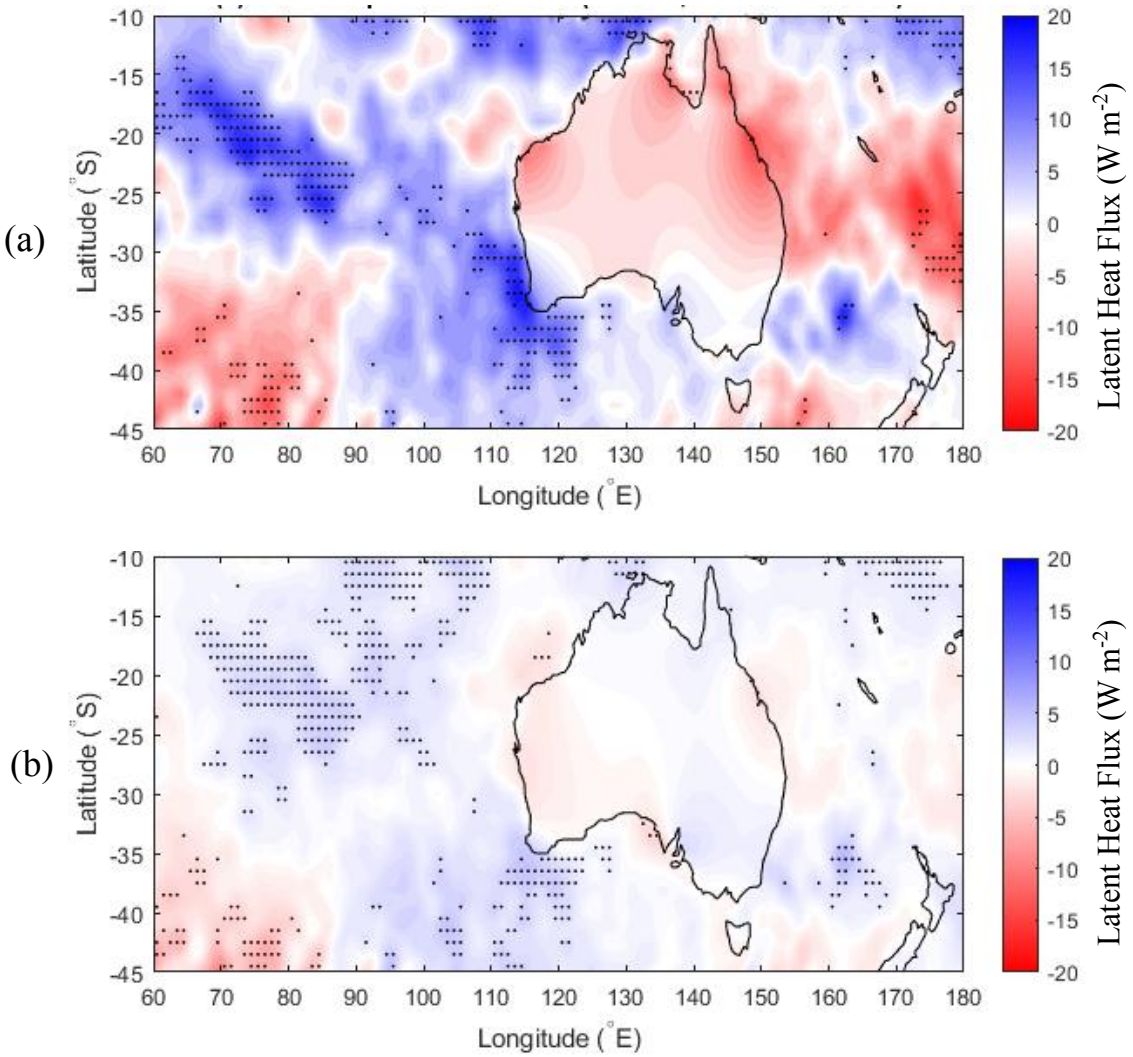

Fig. 6. Composite difference maps of surface heat fluxes between HH and LL years during DJF (1988–2017): (a) Latent Heat Flux (LHF) difference (W/m²), (b) Sensible Heat Flux (SHF) difference (W/m²). Color shading indicates the intensity and sign of the composite anomaly; black hatching denotes regions with statistically significant differences ($p < 0.05$).

3.9 Composite Differences in Thermodynamic and Dynamic Fields (HH–LL)

To diagnose the thermodynamic and dynamic mechanisms driving surface heat flux anomalies, we computed HH–LL composite differences of key variables—specific humidity gradient (Qa–Qs), temperature gradient (Ta–Ts), and zonal/meridional wind components (U, V)—for DJF 1988–2017 (Fig. 7). These composites isolate the effects of coupled IOHP–SPH phases by averaging across years with strong (HH) versus weak (LL) subtropical highs, thereby reducing inter-annual noise and highlighting systematic responses.

Panel (a) shows widespread negative Qa–Qs anomalies (–0.5 to –1.0 g/kg) over the southeastern Indian Ocean, indicating a drier boundary layer that underpins the suppressed latent heat flux observed in Fig. 6. Panel (b) presents positive Ta–Ts anomalies (+0.5 to +1.2 °C), reflecting enhanced atmospheric stability and reduced convective potential, which contribute to spatially structured SHF patterns. Panels (c) and (d) display U and V wind anomalies, revealing strengthened easterlies and anomalous northerly flow that limit moisture transport toward Australia.

By combining thermodynamic gradients with wind overlays, these composites provide a mechanistic link between subtropical high intensity and surface flux modulation, confirming that HH phases correspond to drier, more stable conditions and weaker air–sea interaction. This approach explicitly connects observed surface flux anomalies with both boundary-layer properties and regional circulation dynamics, offering a process-based explanation for the energy redistribution associated with coupled high-pressure systems.

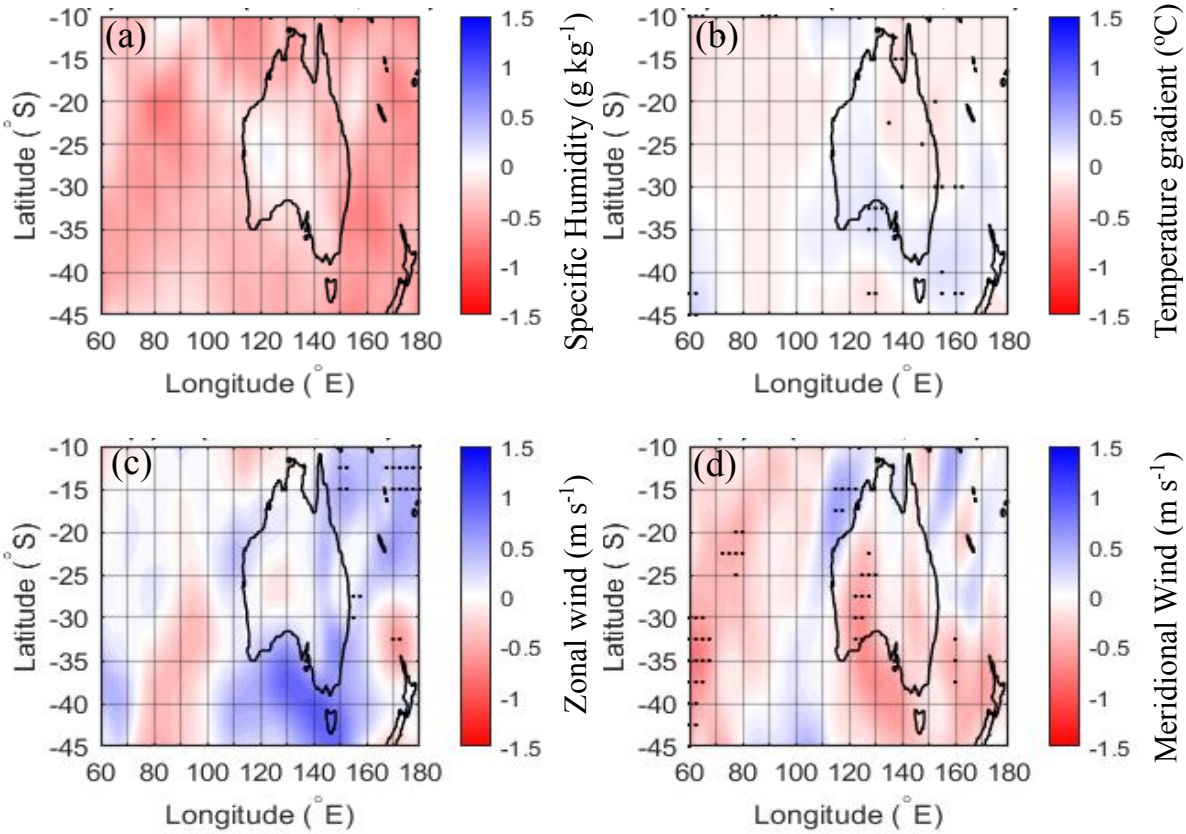

Fig. 7. Composite differences (HH–LL) during DJF (1988–2017) of (a) specific humidity gradient (Qa–Qs; g kg⁻¹), (b) temperature gradient (Ta–Ts; °C), (c) zonal wind (U; m s⁻¹), and (d) meridional wind (V; m s⁻¹). HH years correspond to IOHP–High / SPH–High phases and LL years to IOHP–Low / SPH–Low phases. Negative Qa–Qs and positive Ta–Ts anomalies reflect drier and more stable boundary-layer conditions, while U and V wind anomalies indicate anticyclonic circulation that reduces moisture inflow toward Australia. Stippling denotes grid points significant at $p < 0.05$.

3.10 Thermodynamic Composite Differences with Wind Overlays (DJF)

To better understand the physical mechanisms modulating surface heat fluxes under different IOHP–SPH states, composite differences of key thermodynamic variables—specific humidity (Qa, Qs) and temperature (Ta, Ts)—were computed between HH and LL phases for DJF 1988–2017 and overlaid with wind vectors (U, V) to highlight circulation features (Fig. 8). This approach allows us to link anomalies in surface fluxes directly to both boundary-layer thermodynamics and regional atmospheric circulation, providing a mechanistic interpretation of observed latent and sensible heat patterns.

- **Panel (a):** Qa at 850 hPa shows widespread negative anomalies (–0.5 to –1.0 g/kg) over the southeastern Indian Ocean, reflecting drier mid-tropospheric conditions and subsidence during HH years.

- **Panel (b):** Qs anomalies are weaker but negative along the west coast of Australia, indicating suppressed surface moisture and reduced evaporation.
- **Panel (c):** Ta anomalies (~+0.5 to +1.0 °C) over central and eastern Australia demonstrate enhanced boundary-layer stability and weaker convective mixing.
- **Panel (d):** Ts anomalies show modest cooling near 25–35°S, 90–120°E, linked to wind-driven divergence and reduced surface heat exchange.

The overlaid wind vectors reveal strengthened easterly and southeasterly flow, which limits onshore moisture transport. The spatial coherence between dry, stable thermodynamic anomalies and anticyclonic circulation confirms that HH phases are associated with reduced latent cooling and weaker air–sea interaction. Monte Carlo testing (1000 resamples) identifies regions significant at the 95% confidence level, ensuring that the patterns reflect systematic responses to coupled subtropical highs rather than random variability.

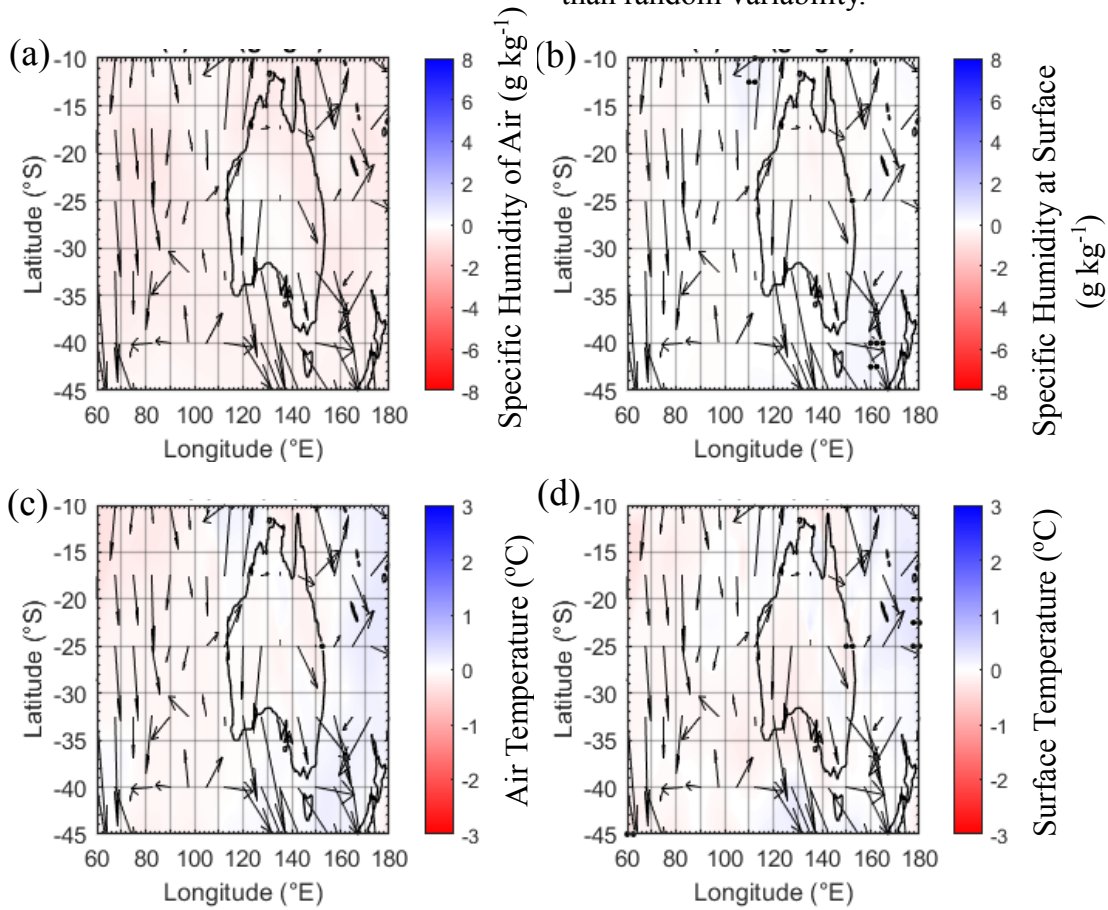

Fig. 8. Composite differences (HH – LL) during DJF (1988–2017) of (a) Specific Humidity of Air (g kg⁻¹), (b) Specific Humidity at the Surface (g kg⁻¹), (c) Air Temperature (°C), and (d) Surface Temperature (°C). Positive anomalies are shown in blue and negative in red. Arrows denote HH–LL wind (U, V) anomalies. Stippling indicates grid points significant at $p < 0.05$.

4. Discussion

The influence of the coupled IOHP–SPH system partly overlaps with major teleconnections. During El Niño events, a weakened Walker circulation coincides with reduced latent heat flux over northern Australia and strengthened IOHP subsidence. Positive SAM phases enhance SPH intensity and sensible heating over southeastern Australia, while negative IOD conditions amplify cross-basin moisture transport. These interactions indicate that large-scale teleconnections modulate, but do not dominate, COA-driven flux variability.

This study applied the Center of Action (COA) framework to examine the joint influence of the IOHP and SPH on surface turbulent heat fluxes over the southeastern Indian Ocean and eastern Australia during DJF (1988–2017). By classifying years into coupled high (HH: IOHP–High/SPH–High) and low (LL: IOHP–Low/SPH–Low) phases, we evaluated composite differences in latent (LHF) and sensible heat fluxes (SHF), as well as supporting anomalies in temperature gradients (Ta–Ts), humidity (Qa-Qs), and wind fields (U, V).

Our results show that during HH phases, the surface energy balance shifts notably. Latent heat flux is strongly reduced (–15 to –25 W/m²), primarily because the boundary layer becomes drier, with negative anomalies in air humidity (Qa ≈ –0.8 g/kg) and surface humidity (Qs ≈ –0.4 g/kg). This reduction in moisture directly suppresses evaporation. In contrast, sensible heat flux over land exhibits a moderate but statistically significant rise (–5 to –10 W/m²), indicating a redistribution of energy from evaporative cooling toward heating the land surface. These changes coincide with a more stable atmosphere: the land–sea temperature difference increases (+0.5 °C to +1.2 °C; Balsamo et al., 2009; Kautz et al., 2022), and easterly to southeasterly winds intensify (–1.5 to –2.0 m/s). Together, this circulation promotes subsidence and limits moisture inflow from surrounding oceans into Australia (Hameed et al., 2011; Pepler et al., 2019; Ur Rehman et al., 2024).

The HH–LL composite analysis of LHF and SHF confirms these patterns, revealing suppressed latent flux and spatially structured sensible flux anomalies over the southeastern Indian Ocean and Australian coastlines (Fig. 6). Further, the thermodynamic composite differences in Qa–Qs and Ta–Ts, overlaid with wind vectors, highlight the physical mechanisms underlying these flux anomalies (Figs. 7–8). Negative humidity gradients and enhanced temperature gradients, combined with strengthened easterly/southeasterly flow, underscore reduced convective mixing and weaker air–sea interaction during HH phases.

Specifically, negative Qa–Qs gradients indicate a drier lower troposphere and reduced evaporation, directly suppressing latent heat flux. In contrast, positive Ta–Ts gradients enhance sensible heat exchange through stronger land–sea thermal contrast and upward heat transfer. These linkages provide a clear physical mechanism connecting thermodynamic anomalies to the observed flux variations under IOHP–SPH coupling.

Bootstrapped Pearson correlations support these interpretations. IOHP exhibits a negative association with seasonal skin temperature ($r = –0.343$, $p = 0.0632$), while SPH shows a moderate positive correlation ($r = 0.368$, $p = 0.0455$), indicating that variations in subtropical highs directly modulate regional thermal conditions. These results align with prior studies demonstrating the broader influence of IOHP and SPH on regional precipitation and air–sea energy fluxes over Australia (Hameed et al., 2011; Ur Rehman et al., 2024).

Overall, the findings reveal that coupled IOHP–SPH states are key regulators of the seasonal surface energy budget. HH phases act to intensify land warming by reducing latent cooling and enhancing sensible heating, providing a process-level explanation for heightened heatwave risk during dry, anticyclonic summers. Moreover, this multi-index diagnostic framework, combining thermodynamic, flux, and circulation analyses, offers a robust approach to monitoring and predicting climate extremes influenced by subtropical highs. Future projections from CMIP6 simulations suggest that these high-pressure systems may shift poleward under greenhouse forcing (Arblaster et al., 2011; IPCC, 2023), potentially extending their influence over southern Australia and intensifying regional heat and drought risks. Monitoring shifts in the strength and position of these high-pressure systems is thus essential for anticipating future heat extremes in a

warming climate (IPCC, 2023; Wang et al., 2024).

These findings also have practical forecasting relevance. Because IOHP–SPH coupling modulates latent and sensible heat exchange several weeks before the onset of heat extremes, its combined index can serve as a potential predictor in seasonal outlooks for Australian heat and drought conditions. Integrating such indices into regional climate models could improve early-warning capability for extreme-temperature events.

These coupled circulation–flux anomalies further explain the occurrence of prolonged heatwaves and drought episodes across southeastern Australia. During persistent HH regimes, reduced latent cooling and enhanced sensible heating amplify land–atmosphere feedbacks, suppress rainfall recovery, and strengthen subsidence-driven warming. Such feedbacks highlight how subtropical anticyclones not only regulate surface energy balance but also modulate the intensity and duration of regional heat extremes.

5. Conclusion

This study highlights the significant role of the coupled IOHP–SPH system in shaping DJF surface energy balance over the southeastern Indian Ocean and eastern Australia during 1988–2017. HH phases suppress LHF through reduced near-surface humidity while enhancing SHF due to stronger land–sea thermal contrast. Strengthened easterly–southeasterly flow further limits moisture transport and reinforces atmospheric stability.

These findings demonstrate that variability of IOHP-SPH system influences regional heat extremes by favoring warmer and drier boundary layer conditions and modifying the transfer of latent and sensible heating. As changes triggered within the coupled highs impact surface fluxes several weeks before an event occurs, there is evidence that the IOHP-SPH index can be useful as a predictor for summer heat and drought conditions. Projections based on CMIP6 models that show a poleward intensification of subtropical high pressure suggest an amplified influence on Australian heat extremes.

Accordingly, it is imperative to monitor changes occurring with respect to the strength and location of IOHP and SPH with the intention of improving early warning and risk estimation with regard to future climate change.

Authors' Contribution

Nasir Ilyas conceived the research idea, designed the methodology, performed the data analysis, prepared all figures, and led the manuscript writing and revisions. Muhammad Jawed Iqbal assisted in methodological refinement, contributed to scientific interpretation, and provided critical review and proofreading of the manuscript.

Data Availability Statement

Datasets used in this study are publicly available from OAFlux and NCEP/NCAR Reanalysis repositories as cited.

Conflicts of Interest

The authors declare no conflict of interest.

Declaration of Funding

This research received no specific funding from any public, commercial, or not-for-profit agencies.

References

Alexander, L. V., & Arblaster, J. M. (2009). Assessing trends in observed and modelled climate extremes over Australia in relation to future projections. *International Journal of Climatology*, *29*(3), 417–435. https://doi.org/10.1002/joc.1730

Arblaster, J. M., Meehl, G. A., & Karoly, D. J. (2011). Future climate change in the Southern Hemisphere: Competing effects of ozone and greenhouse gases. *Geophysical Research Letters*, *38*(2), L02701, https://doi.org/10.1029/2010GL045384

Balsamo, G., Beljaars, A., Scipal, K., Viterbo, P., van den Hurk, B., Hirschi, M., & Betts, A. K. (2009). A Revised Hydrology for the ECMWF Model: Verification from Field Site to Terrestrial Water Storage and Impact in the Integrated Forecast System. *Journal of Hydrometeorology*, *10*(3), 623–643. https://doi.org/10.1175/2008JHM1068.1

Hameed, S., Iqbal, M., Saqib-ur, R., & Collins, D. (2011). Impact of the Indian Ocean high-pressure system on winter precipitation over western and southwestern Australia. *Australian Meteorological and Oceanographic Journal*, *61*(3), 159–170. https://doi.org/10.22499/2.6103.002

Holbrook, N. J., Scannell, H. A., Sen Gupta, A., Benthuysen, J. A., Feng, M., Oliver, E. C. J., Alexander, L. V., Burrows, M. T., Donat, M. G., Hobday, A. J., Moore, P. J., Perkins-Kirkpatrick, S. E., Smale, D. A., Straub, S. C., & Wernberg, T. (2019). A global assessment of marine heatwaves and their drivers. *Nature Communications*, *10*(1), 2624. https://doi.org/10.1038/s41467-019-10206-z

Holbrook, N. J., Hernaman, V., Koshiba, S., Lako, J., Kajtar, J. B., Amosa, P., & Singh, A. (2022). Impacts of marine heatwaves on tropical western and central Pacific Island nations and their communities. *Global and Planetary Change*, *208*, 103680. https://doi.org/10.1016/j.gloplacha.2021.103680

IPCC. (2023). Weather and Climate Extreme Events in a Changing Climate. In *Climate Change 2021 – The Physical Science Basis* (pp. 1513–1766). Cambridge University Press. https://doi.org/10.1017/9781009157896.013

Kalnay, E., Kanamitsu, M., Kistler, R., Collins, W., Deaven, D., Gandin, L., Iredell, M., Saha, S., White, G., Woollen, J., Zhu, Y., Leetmaa, A., Reynolds, R., Chelliah, M., Ebisuzaki, W., Higgins, W., Janowiak, J., Mo, K. C., Ropelewski, C., … Joseph, D. (1996). The NCEP/NCAR 40-Year Reanalysis Project. *Bulletin of the American Meteorological Society*, *77*(3), 437–471. https://doi.org/10.1175/1520-0477(1996)077<0437:TNYRP>2.0.CO;2

Kautz, L.-A., Martius, O., Pfahl, S., Pinto, J. G., Ramos, A. M., Sousa, P. M., & Woollings, T. (2022). Atmospheric blocking and weather extremes over the Euro-Atlantic sector – a review. *Weather and Climate Dynamics*, *3*(1), 305–336. https://doi.org/10.5194/wcd-3-305-2022.

Khan, M. A., Khattak, M. S., & Khan, A. (2022). Selection of the Most Suitable Gridded Precipitation and Temperature Datasets for the Kabul River Basin based on Statistical Indices - A Transboundary Basin between Pakistan and Afghanistan. *Journal of Himalayan Earth Sciences*, *55*(1), 50–66.

Khattak, M. S., & Ali, S. (2015). Assessment of temperature and rainfall trends in Punjab province of Pakistan for the period 1961-2014. *Journal of Himalayan Earth Sciences 48*(2), 42–61.

Lewis, S. C., King, A. D., & Perkins-Kirkpatrick, S. E. (2017). Defining a New Normal for Extremes in a Warming World. *Bulletin of the American Meteorological Society*, *98*(6), 1139–1151. https://doi.org/10.1175/BAMS-D-16-0183.1

Marshall, G. J. (2003). Trends in the Southern Annular Mode from Observations and Reanalyses. *Journal of Climate*, *16*(24). https://doi.org/10.1175/1520-0442(2003)016<4134:TITSAM>2.0.CO;2

Pepler, A., Dowdy, A., & Hope, P. (2019). A global climatology of surface anticyclones, their variability, associated drivers and long-term trends. *Climate Dynamics*, *52*(9–10), 5397–5412. https://doi.org/10.1007/s00382-018-4451-5

Pepler, A., Timbal, B., Rakich, C., & Coutts-Smith, A. (2014). Indian Ocean Dipole Overrides ENSO's Influence on Cool Season Rainfall across the Eastern Seaboard of Australia. *Journal of Climate*, *27*(10), 3816–3826. https://doi.org/10.1175/JCLI-D-13-00554.1

Romanski, J., & Hameed, S. (2015). The Impact of Trends in the Large Scale Atmospheric Circulation on Mediterranean Surface Turbulent Heat Fluxes. *Advances in Meteorology*, *2015*. https://doi.org/10.1155/2015/519593

Saji, N. H., Goswami, B. N., Vinayachandran, P. N., & Yamagata, T. (1999). A dipole mode in the tropical Indian Ocean. *Nature*, *401*(6751). https://doi.org/10.1038/43854

Trenberth, K. E., & Fasullo, J. T. (2012). Tracking Earth's Energy: From El Niño to Global Warming. *Surveys in Geophysics*, *33*(3–4), 413–426. https://doi.org/10.1007/s10712-011-9150-2

Ur Rehman, S., Simmonds, I., Usmani, B. A., & Hannachi, A. (2024). The role played by the Indian Ocean High in affecting winter precipitation over Victoria, Australia. *Dynamics of Atmospheres and Oceans*, *107*, 101484. https://doi.org/10.1016/j.dynatmoce.2024.101484

Wang, Z., Jing, Z., & Song, F. (2024). Weakened large-scale surface heat flux feedback at midlatitudes under global warming. *Nature Communications*, *15*(1), 10020. https://doi.org/10.1038/s41467-024-54394-9

Wilks, D. S. (2016). The Stippling Shows Statistically Significant Grid Points: How Research Results are Routinely Overstated and Overinterpreted, and What to Do about It. *Bulletin of the American Meteorological Society*, *97*(12), 2263–2273. https://doi.org/10.1175/BAMS-D-15-00267.1

Yaseen, M., Rientjes, T., Nabi, G., Mughal, H.-U.-R., & Latif, M. (2015). Assessment of recent temperature trends in Mangla watershed. *Journal of Himalayan Earth Sciences*, *48*(2), 42–61.

Yu, L., & Weller, R. A. (2007). Objectively Analyzed Air–Sea Heat Fluxes for the Global Ice-Free Oceans (1981–2005). *Bulletin of the American Meteorological Society*, *88*(4). https://doi.org/10.1175/BAMS-88-4-527

Zhang, Y., Wallace, J. M., & Battisti, D. S. (1997). ENSO-like Interdecadal Variability: 1900–93. *Journal of Climate*, *10*(5), 1004–1020. https://doi.org/10.1175/1520-0442(1997)010<1004:ELIV>2.0.CO;2

Zhao, Z., & Wang, Y. (2017). Influence of the West Pacific subtropical high on surface ozone daily variability in summertime over eastern China. *Atmospheric Environment*, *170*, 197–204. https://doi.org/10.1016/j.atmosenv.2017.09.024